Paleoceanography and Paleoclimatology

Supporting Information for

Data-model comparisons of tropical hydroclimate changes over the Common Era

A. R. Atwood[1*], D. S. Battisti[2], E. Wu[2], D. M. W. Frierson[2], J. P. Sachs[3]

[1] *Florida State University, Dept. of Earth Ocean and Atmospheric Science, Tallahassee, FL, USA*

[2] *University of Washington, Dept. of Atmospheric Sciences, Seattle, WA 98195, USA*

[3] *University of Washington, School of Oceanography, Seattle, WA 98195, USA*

Contents of this file

Text S1. Monsoon Responses to Orbital Forcing in CESM

Orbital forcing during the last millennium was primarily due to changes in precession. From 850 CE to the present, a 20-day shift in perihelion (from 15 December to 4 January) occurred, leading to a decrease in insolation in the second half of the year (June to December relative to the first half of the year (January to May; Fig. S2). Over the last millennium, insolation in the NH high latitudes declined from July-September (late boreal summer and fall) by ~3 Wm^{-2}, and declined in the SH high latitudes from October-December (late austral spring and summer), by a similar magnitude (Schmidt et al. 2011).

In CESM, orbital forcing causes the NH monsoon systems of South Asia and West Africa to weaken in association with strong cooling across the NH continents (including Asia and North Africa) during boreal summer and fall (Fig. 5). These features are present, though more muted, in the all-forcing CESM simulations and in the CMIP5/PMIP3 simulations (Fig. 4), indicating an important role for orbital forcing in driving the forced long-term tropical hydroclimate response over the last millennium in the models. In the model runs, the lower late summer and early fall insolation cools the NH high latitudes, which is conducive to the development of more extensive and thicker sea ice going into boreal winter. The resultant cooling of the NH extratropics is most pronounced over land (due to differences in the partitioning of sensible and latent heating over land and water) and thus gives rise to reduced land-sea temperature contrast between Asia and the Indo-Pacific in boreal summer and fall. The same feature is found in the West African monsoon–i.e. enhanced cooling of northern Africa in boreal summer and fall leads to weaker temperature contrast between West Africa and the tropical Atlantic and a weakening of the West African monsoon. This cooling also extends into the NH extratropical oceans and over parts of the tropical oceans, including the northern tropical Atlantic, where enhanced cooling during the onset of the South American monsoon season in austral spring (SON) gives rise to an anomalous meridional SST gradient in the tropical Atlantic, shifting rainfall southward over the equatorial Atlantic Ocean and into the South American monsoon entrance region (Fig. S6).

Text S2: Zonally-averaged precipitation changes and cross-equatorial heat transport

Despite the large data-model disagreement in regional precipitation changes over the last millennium, some coherency is observed in the zonally averaged context: all CMIP5/PMIP3 models demonstrate a small zonal mean southward shift in tropical precipitation (ΔP_{NH-SH}) during the LIA and a decrease in the cross-equatorial atmospheric energy transport ($\Delta AHT_{\phi=0}$), as expected from energetic arguments (Fig. 7; Donohoe et al., 2013; Kang et al., 2008). The decreased cross-equatorial atmospheric energy transport is associated with greater cooling of the NH atmosphere through vertical energy fluxes during the LIA. Possible sources of this hemispheric asymmetry in atmospheric cooling include asymmetric climate forcings (e.g. volcanic forcing), symmetric forcings (due to the seasonal cycle in planetary albedo), and/or asymmetry in the climate feedbacks, including those associated with changes in surface albedo and clouds. In addition, asymmetry in the surface energy fluxes (e.g. through a change in the Atlantic Meridional Overturning Circulation) could lead to asymmetric atmospheric cooling.

Our energy budget analysis with the single layer atmosphere radiation model (the APRP analysis) indicates that the southward tropical precipitation shift occurs in tandem with anomalous northward atmospheric energy transport that is primarily driven by volcanic forcing (i.e. greater volcanic aerosol loading in the northern hemisphere), and secondarily by land use changes (i.e. cropland expansion in Eurasia) and by the surface albedo feedback (e.g. through the growth of Arctic sea ice in response to precessional forcing; Fig. S13). Of the LW feedbacks, the lapse rate feedback is the largest positive feedback. Although both hemispheres experience greater cooling near the surface than aloft poleward of around 30º-40º latitude, these lapse rate changes are substantially larger in the Northern Hemisphere than the Southern Hemisphere (see Fig. S2 in Atwood et al., 2016), likely due to a combination of land-use forcing, increased high-latitude snow cover and sea ice in the Northern Hemisphere, and the greater land area in the Northern Hemisphere (as it is easier to have surface-trapped cooling over land, especially in winter). LW cloud and water vapor feedbacks also contribute to greater cooling of the Northern Hemisphere. The positive LW water vapor feedback occurs in response to the lower atmospheric water vapor concentration in the Northern Hemisphere (the saturation vapor pressure decreases as the atmosphere cools, as given by the Clausius–Clapeyron equation). In addition, the SW water vapor feedback represents a small additional positive feedback in all of the models, consistent with lower absorption of incoming SW radiation by atmospheric water vapor in the cooler Northern Hemisphere.

The net forcing displays larger hemispheric asymmetry in the second half of the LIA in all models, due to larger asymmetry in both the volcanic and land use forcings. During the earlier half of the LIA, however, changes in ocean heat transport (OHT) generally reinforce the asymmetry imposed by the forcings and shortwave feedbacks, and in the two GISS simulations, these OHT changes are larger than the combined forcing (Fig. S13). Ultimately, however, the net change in cross-equatorial atmospheric heat transport is modest ($\leq$ -0.2 W/m^2) throughout the LIA in all models, because the hemispheric asymmetry imposed by the forcings and positive feedbacks is opposed by changes in outgoing longwave radiation associated with greater cooling of the NH (i.e. the Planck feedback).

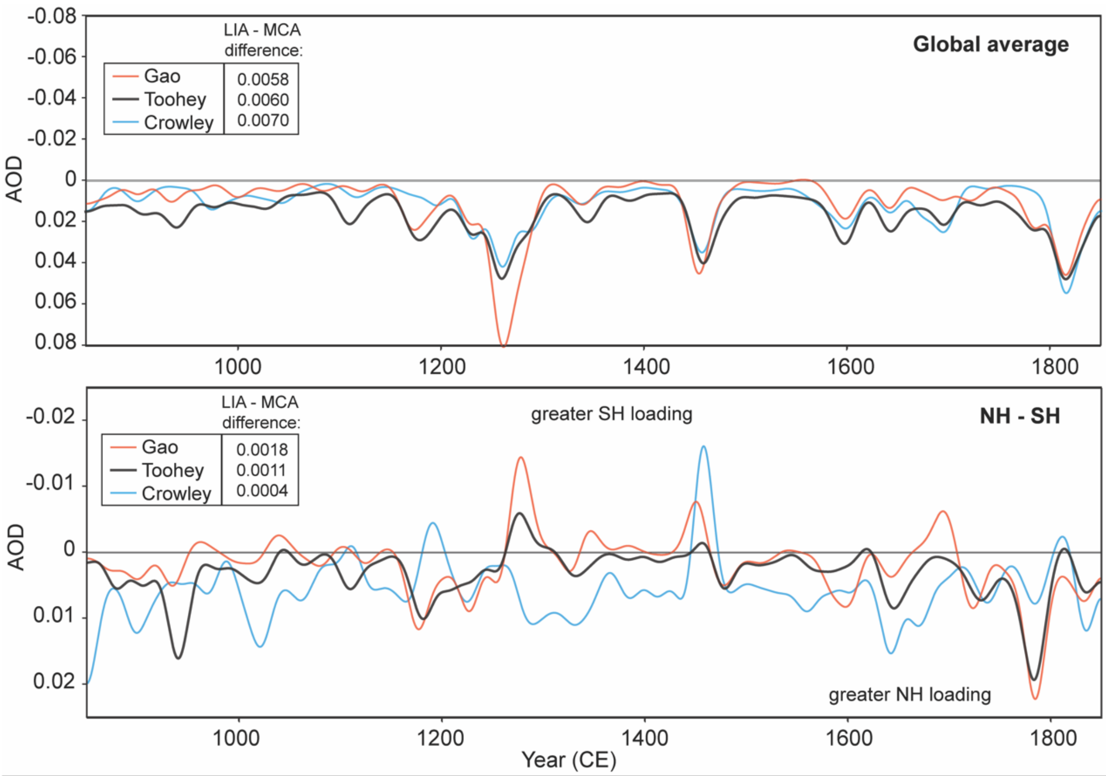

Figure S1. Volcanic aerosol forcing over the last millennium, represented in terms of the stratospheric aerosol optical depth (AOD) from Crowley et al. (2008), Gao et al. (2008), and Toohey et al. (2017). For Gao et al. (2008), AOD was estimated from the sulfate loading by dividing the loading by 150 Tg (Schmidt et al., 2011). The globally averaged AOD (top) and hemispheric asymmetry (bottom) were filtered using a Gaussian filter (σ = 10 years). The differences in AOD averaged over the LIA (1450-1850 CE) minus the MCA (950-1200 CE) are shown in the legends.

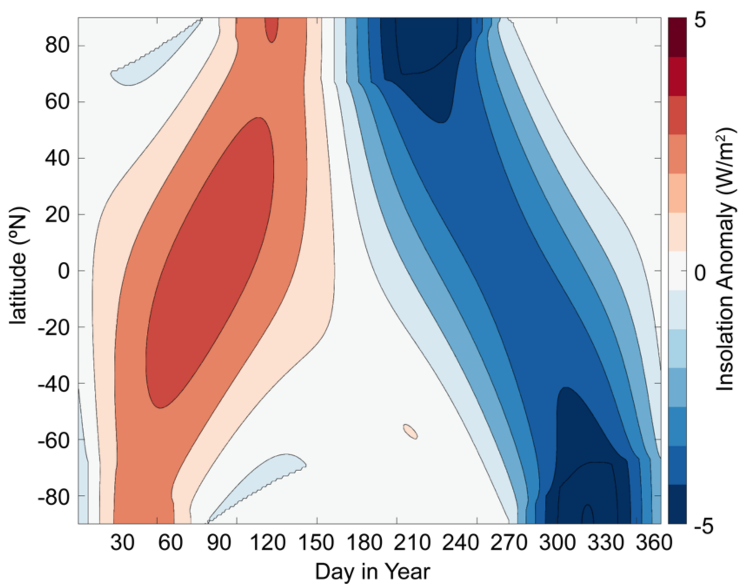

Figure S2. Insolation difference between the LIA (1450-1850 CE) and MCA (950-1200 CE) in W/m^2 as a function of latitude and Julian day. Data were derived from the Berger et al. (1978) equations.

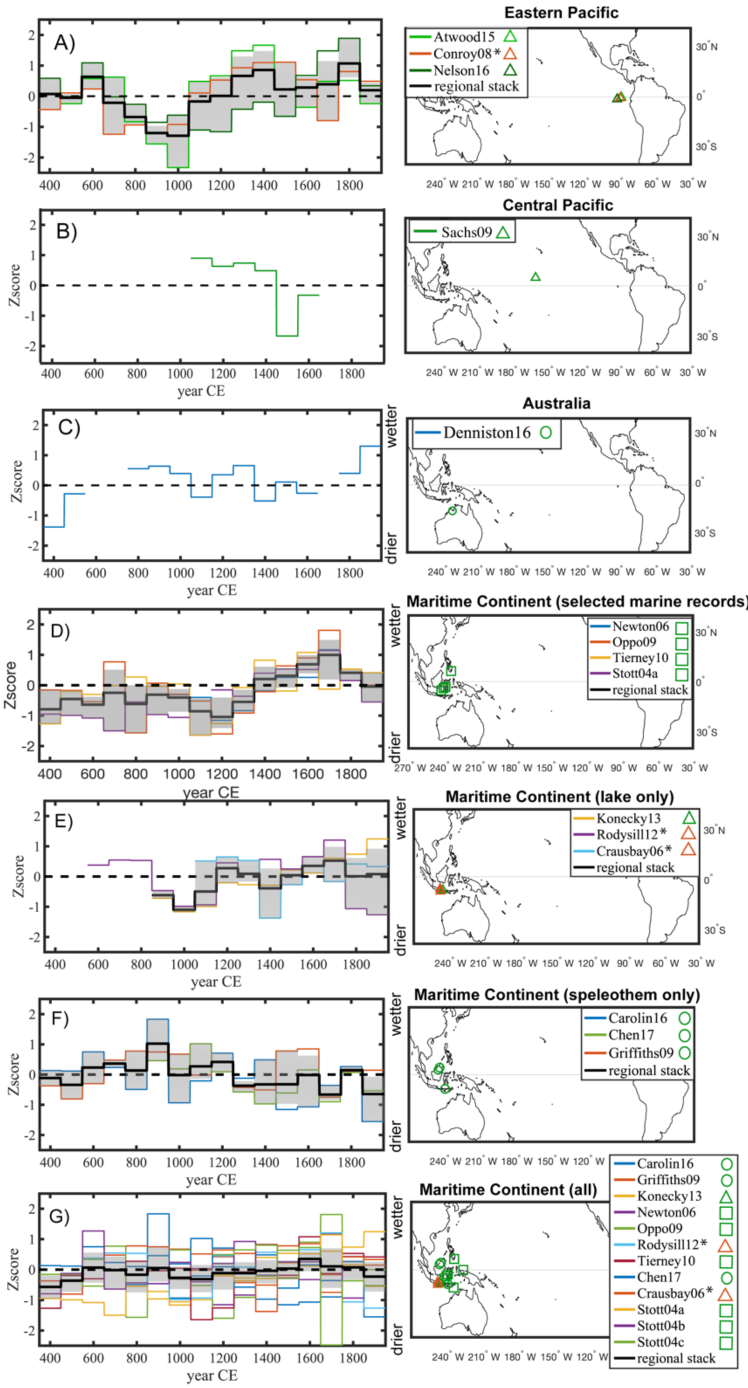

Figure S3. Regional compilations of the tropical hydroclimate reconstructions from 350-1850 CE, converted into Z-scores and averaged over 100-year bins (as in Fig. 3). (A-B) The eastern and central Pacific records plotted separately, (C) the northern Australian record, (D) the four marine records from the Makassar Strait and the Philippine Islands, (E) all lake records from the Maritime Continent, (F) all speleothem records from the Maritime Continent, (G) all records (marine and terrestrial) from the Maritime Continent. For all records, higher Z-scores indicate wetter conditions, based on interpretation in the original study (from Table 1). The average and standard deviation of all records in each region is depicted by the black line and shading, respectively. The maps indicate the location of the records, where the symbol denotes the type of proxy archive (circle = speleothem, triangle = lake, square = marine sediment, diamond = ice) and the color and asterisk indicates whether the record is based on water isotopes (green) or not (orange and asterisk).

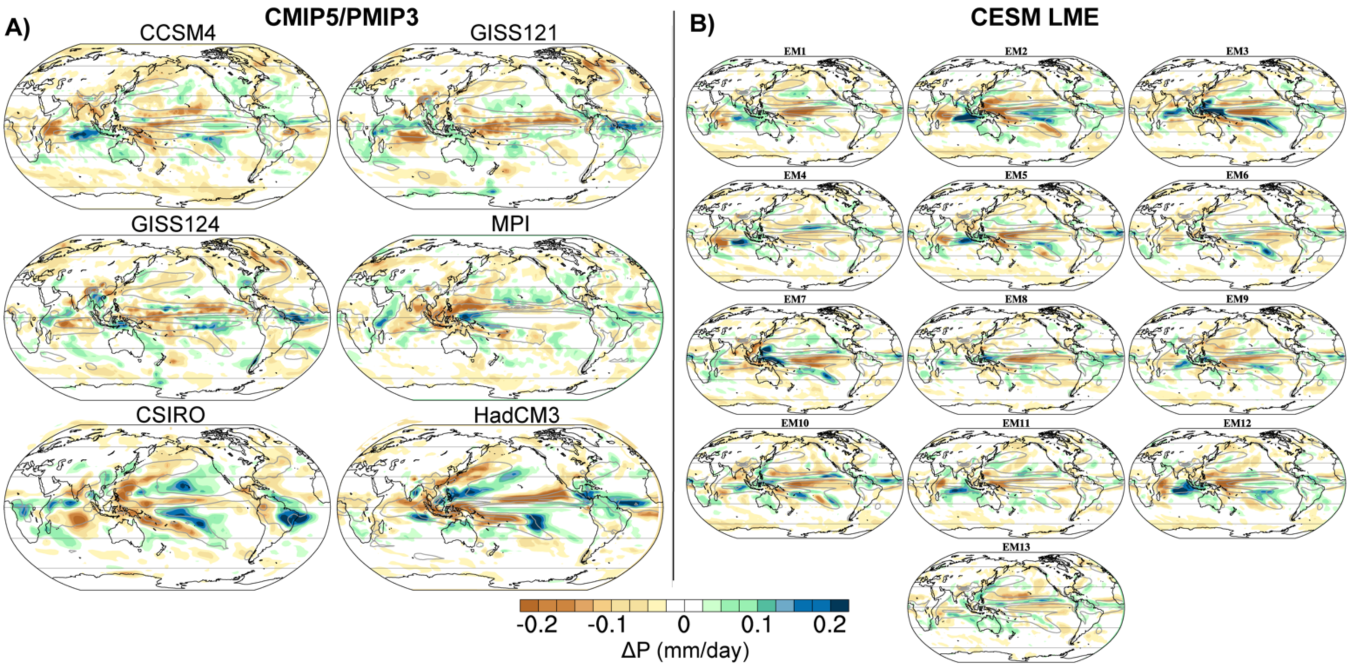

Figure S4. Change in mean annual precipitation in the individual A) CMIP5/PMIP3 last millennium simulations and B) CESM Last Millennium Ensemble simulations during the LIA (1450-1850 CE) relative to the MCA (950-1200 CE) (colors) overlaid on contours of mean annual precipitation over the MCA.

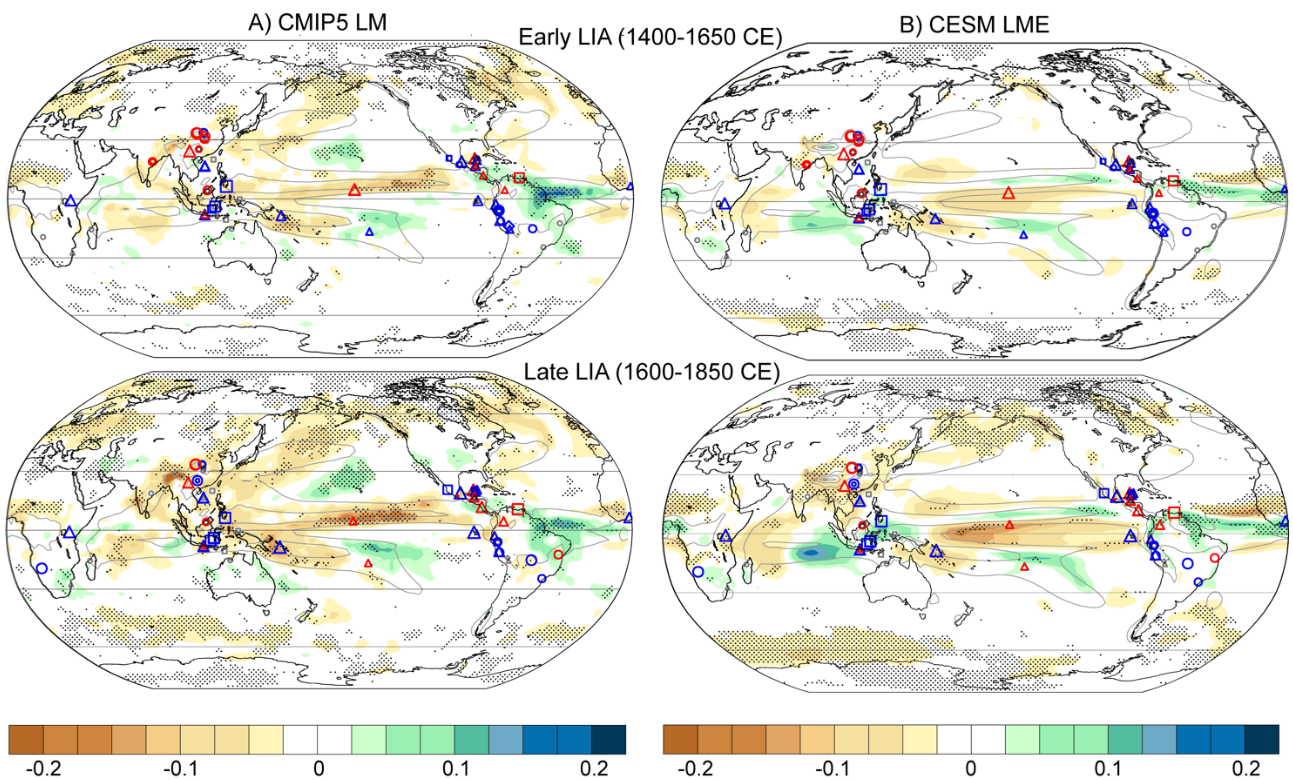

Figure S5. As in Fig. 4 of the main text but for different definitions of the LIA. The early LIA (1400-1650 CE) is shown in the top panels and the late LIA (1600-1850 CE) is shown in the bottom panels.

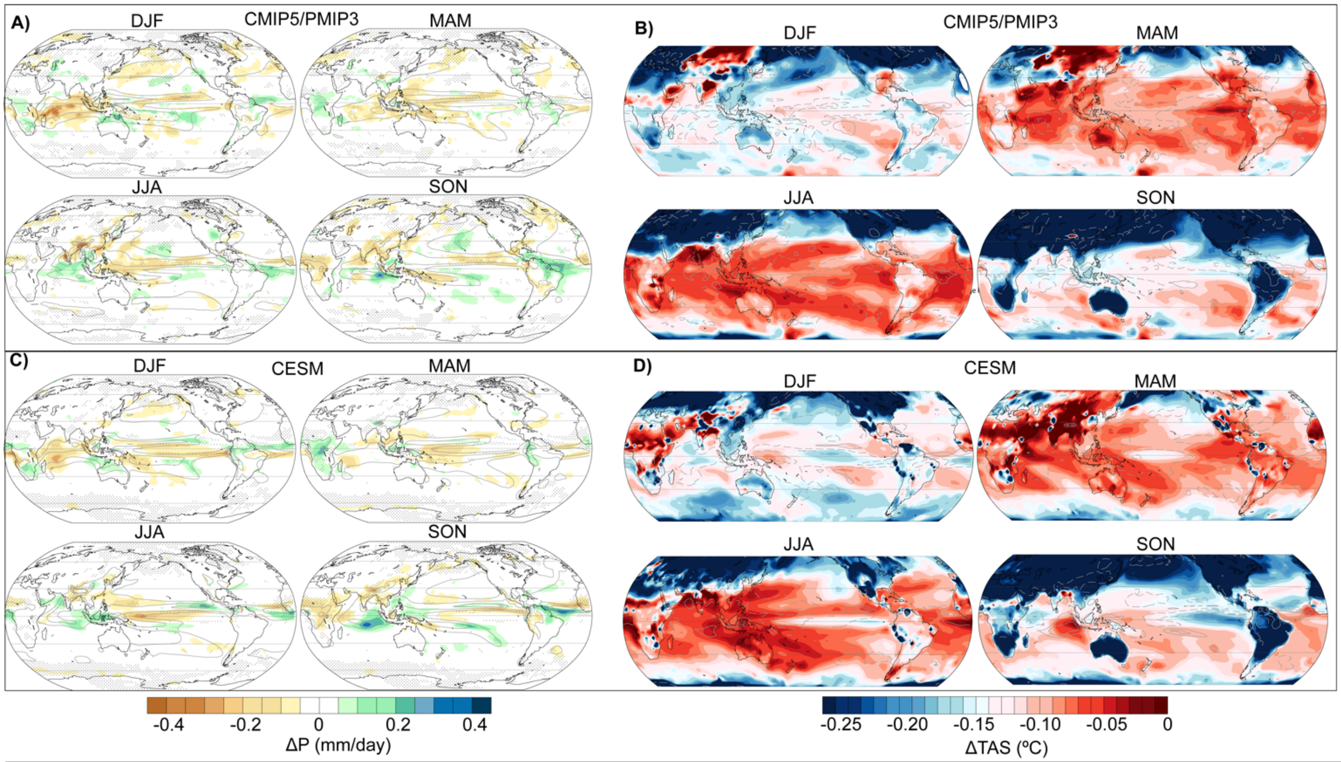

Figure S6. (A,C) Seasonal climatology of the multi-model mean change in precipitation (colors) during the LIA (1400-1650 CE) relative to the MCA (950-1200 CE) in A) the PMIP3/CMIP5 last millennium simulations and C) the CESM Last Millennium Ensemble simulations. Unfilled contours indicate the mean annual precipitation over the MCA in the respective simulations (contour interval 4 mm/day). Stippling indicates where ≥ 80% of the models agree on the sign of the change. (B,D) Seasonal climatology of the multi-model mean change in surface air temperature (colors) during the same period. Unfilled contours indicate the change in precipitation; contour interval is 0.15 mm/day, solid (dashed) contours represent positive (negative) anomalies.

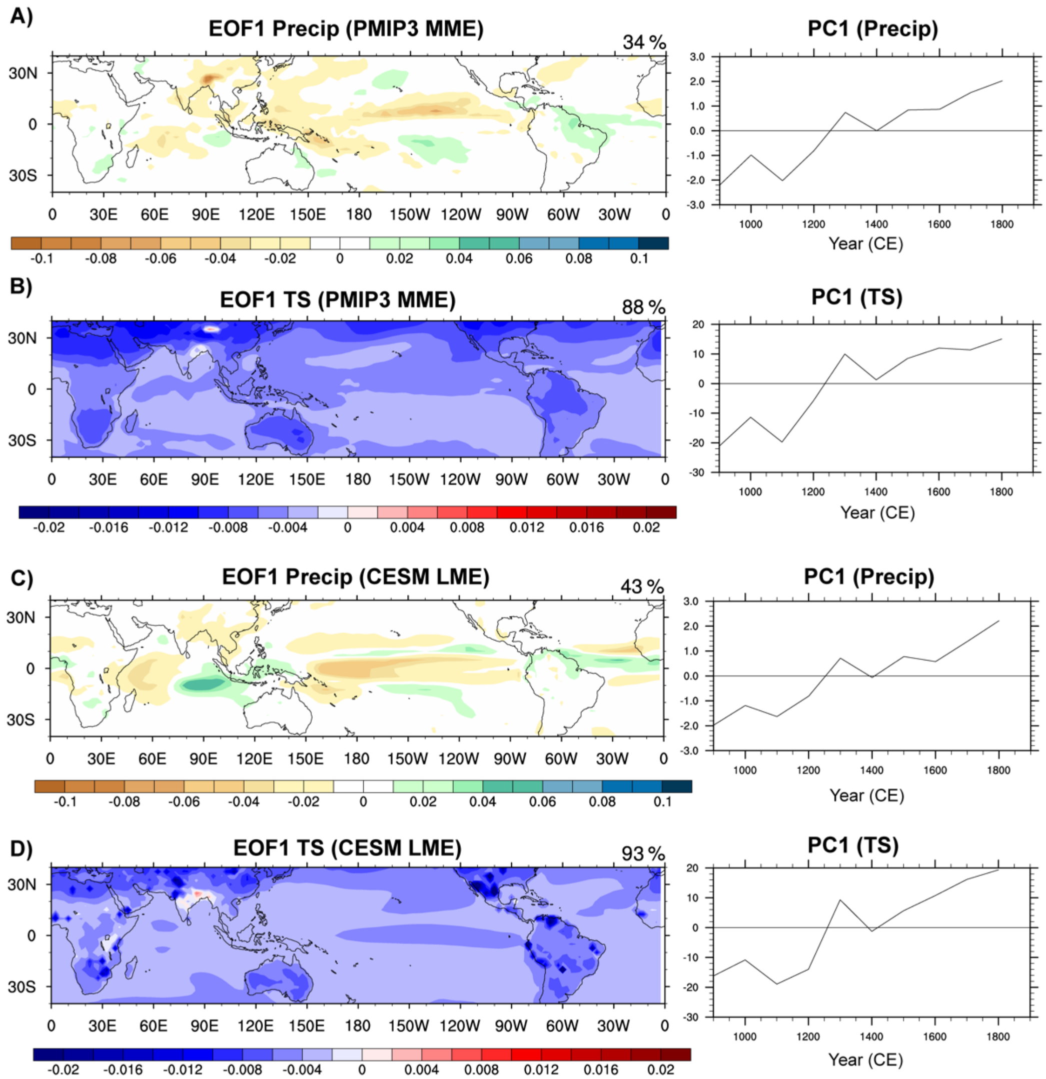

Figure S7. Normalized EOF 1 loadings and PC 1 of the CMIP5/PMIP3 multi-model mean and CESM ensemble mean tropical precipitation and surface temperature (TS), binned into 100-yr windows prior to EOF analysis (A) CMIP5/PMIP3 precipitation, (B) CMIP5/PMIP3 surface temperature, (C) CESM precipitation, (D) CESM surface temperature.

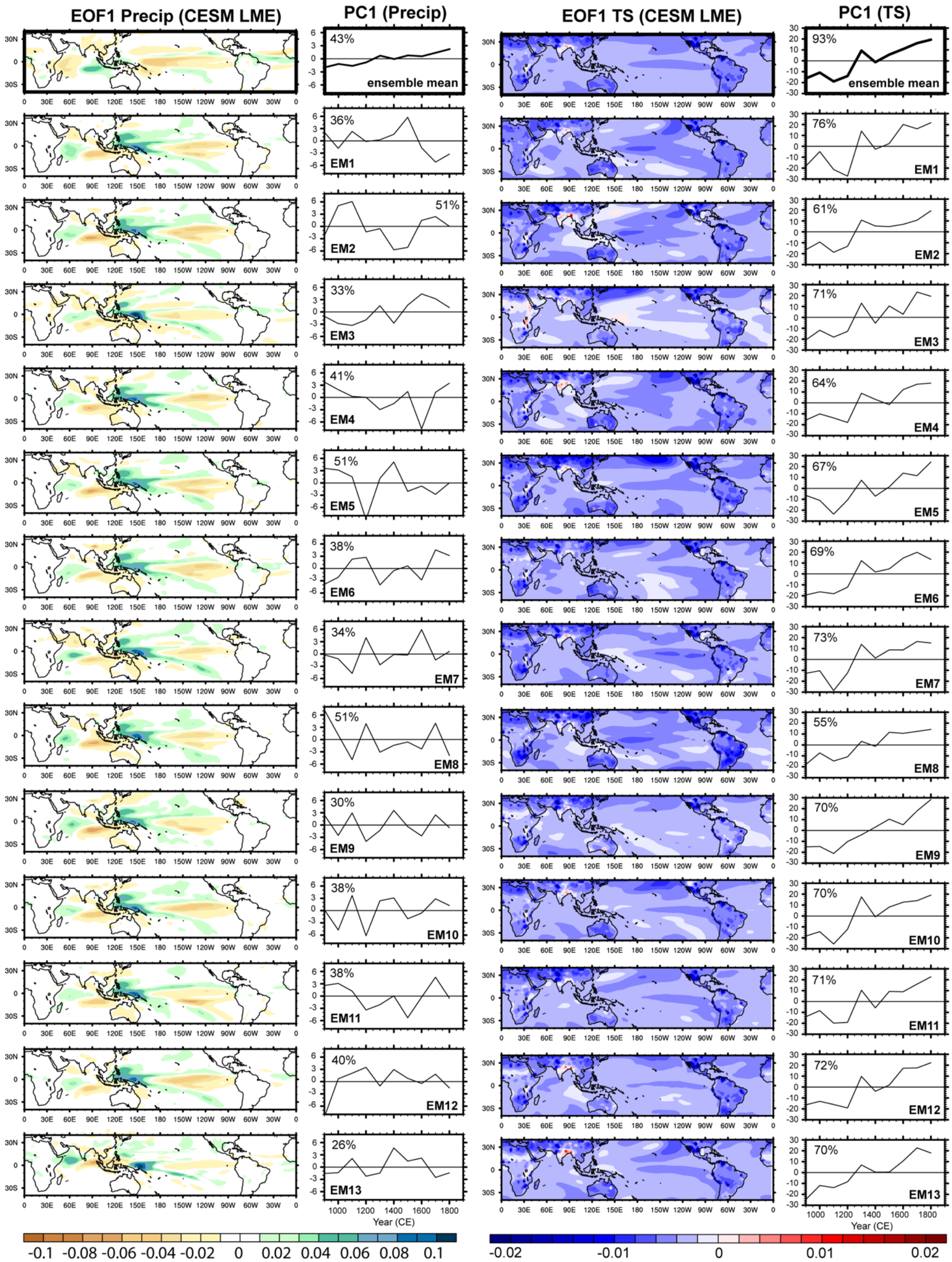

Figure S8. Normalized EOF 1/ PC 1 of tropical precipitation (left two panels) and surface temperature (right two panels) in each of the CESM LME full forcing ensemble members and the ensemble mean (MME). The data were binned into 100-yr windows prior to EOF analysis.

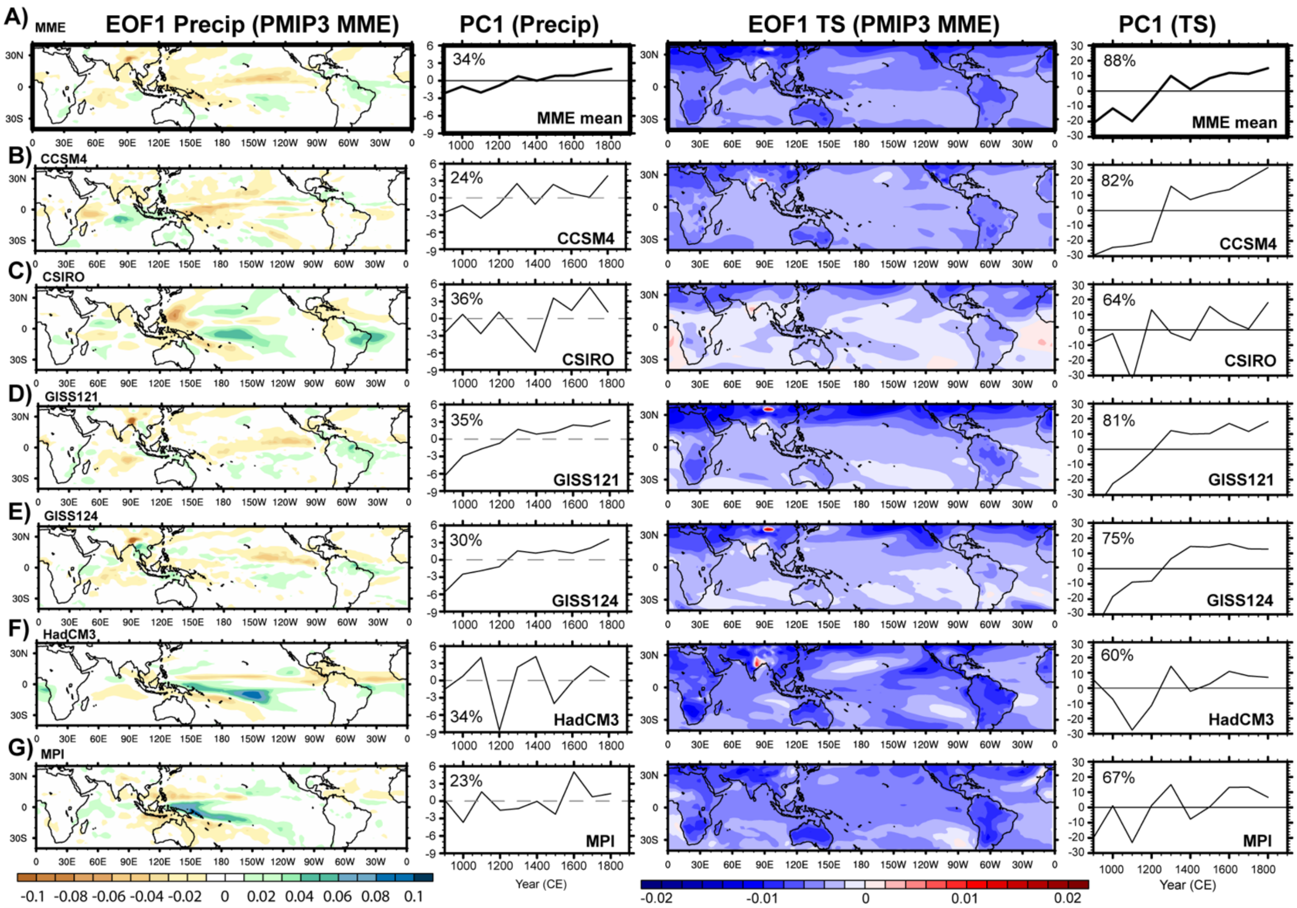

Figure S9. As in Fig. S8 but for each of the CMIP5/PMIP3 last millennium simulations and the multi-model mean (MME). The data were binned into 100-yr windows prior to EOF analysis.

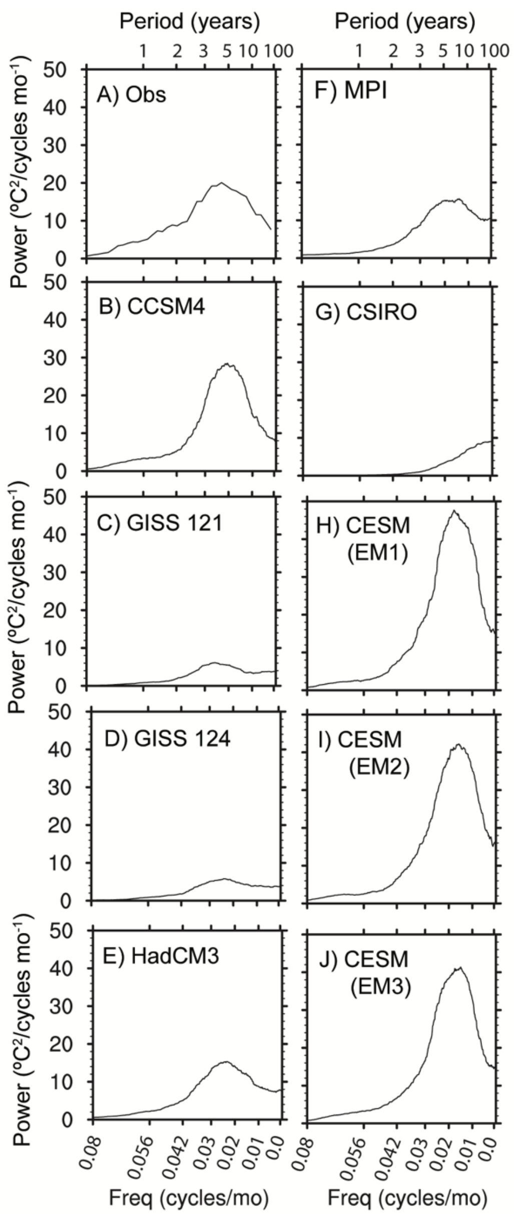

Figure S10. Power spectra of 3-month running mean Niňo 3 SSTAs in (A) observations (ERSST v3b; 1971-2010), (B-G) the CMIP5/PMIP3 last millennium simulations, and (H-J) ensemble members 1-3 of the CESM LME. The power spectra were computed using a forward Fast Fourier Transform. Periodogram estimates were averaged together using modified Daniell smoothing with weights 1/13 for the observational data and 1/213 for the model data.

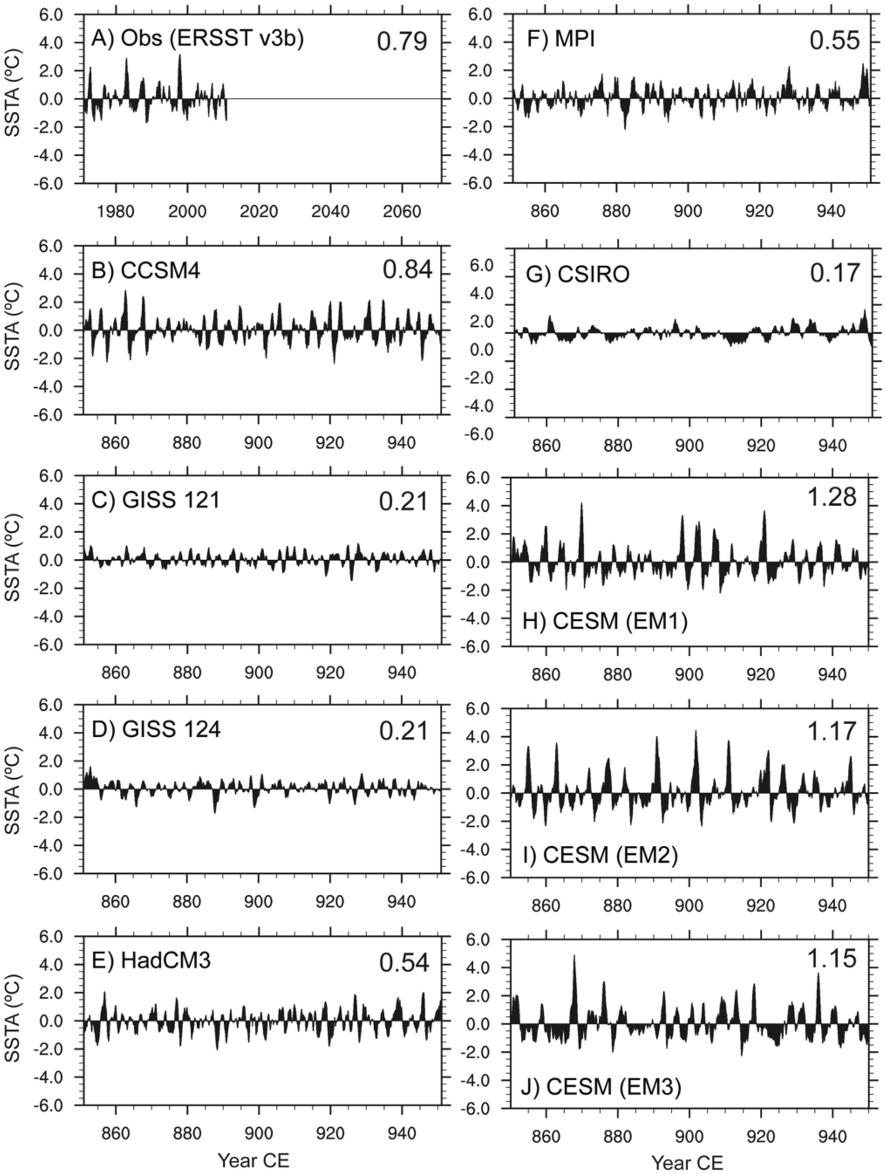

Figure S11. Time series of 3-month running mean Niño 3 SSTAs in (A) observations (ERSST v3b; 1971-2010), (B-G) the first 100 years of the CMIP5/PMIP3 last millennium simulations, and (H-J) the first 100 years of ensemble members 1-3 of the CESM LME. The variance of each time series (1971-2010 for the observations and all 1,000 years of the model simulations) is indicated in the right corner of each panel.

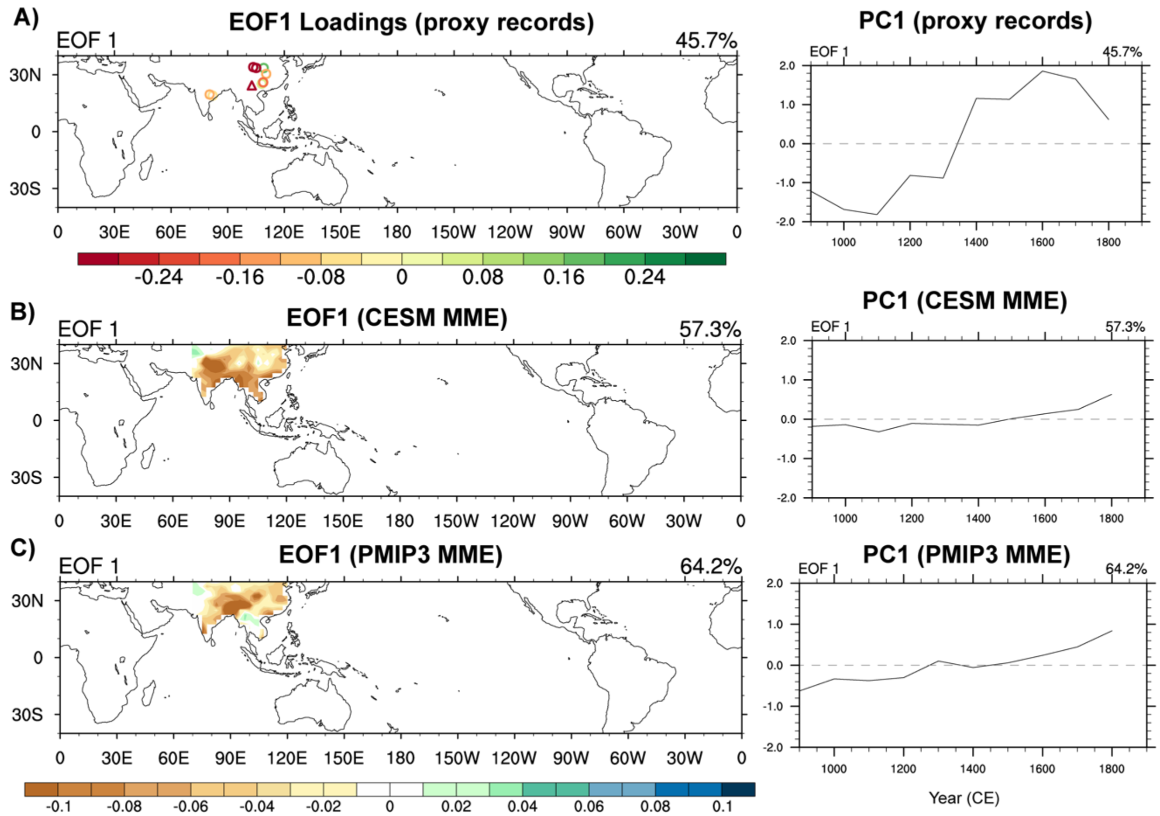

Figure S12. Normalized EOF1 loadings and PC1 for A) proxy data (Z scores) and (B,C) precipitation over Asia in the CESM LME (ensemble mean) and the PMIP3 ensemble mean. The proxy and model data were binned into 100-yr windows prior to EOF analysis. Higher values of the loadings indicate wetter (more isotopically depleted) conditions.

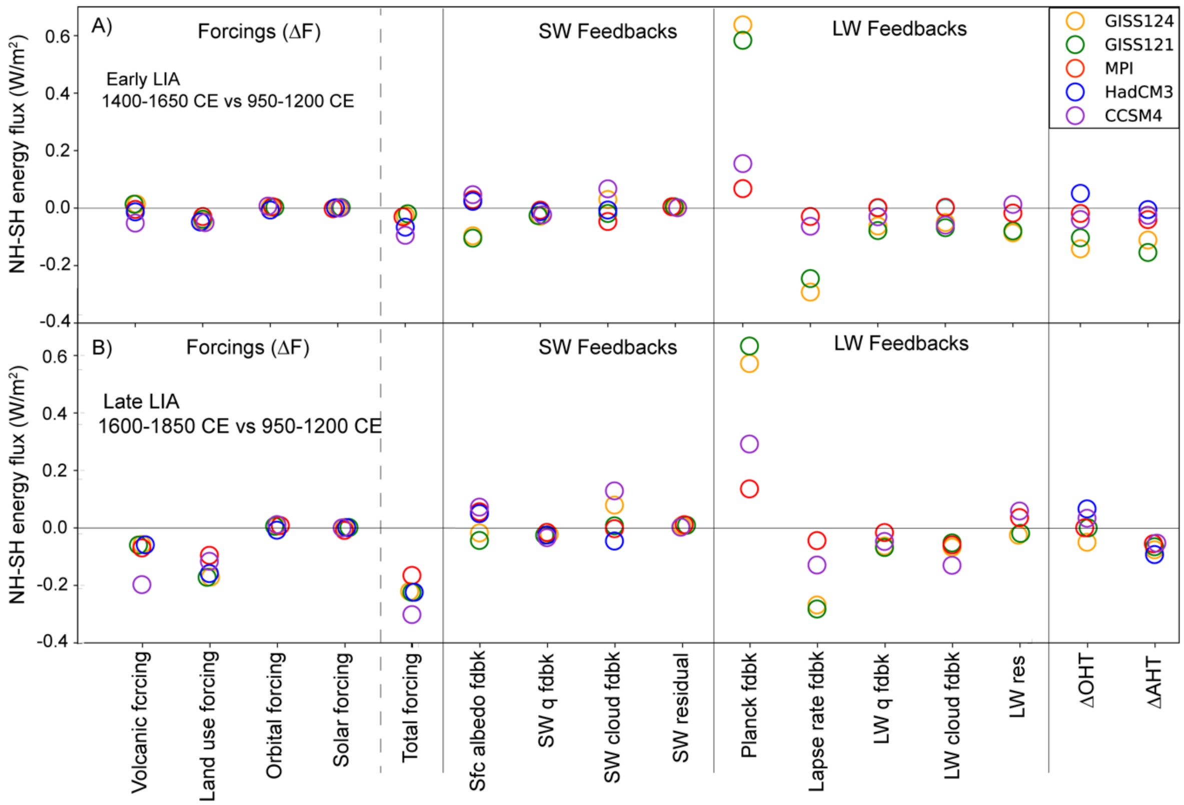

Figure S13. Difference in Northern Hemisphere minus Southern Hemisphere vertical energy fluxes into the atmosphere during the first (1400-1650 CE) and second (1600-1850 CE) half of the LIA relative to the MWP (950-1200 CE) due to contributions from: SW and LW forcings (volcanic, land use, solar, greenhouse gas), SW feedbacks (surface albedo, SW water vapor (q), SW cloud, SW residual), and LW feedbacks (Planck, lapse rate, LW water vapor (q), LW cloud, LW residual). The difference in Northern Hemisphere minus Southern Hemisphere surface energy flux (OHT) and net change in vertical atmospheric energy flux (AHT) is also plotted. Negative values indicate a decrease in atmospheric energy flux in the Northern Hemisphere relative to the Southern Hemisphere. See Methods and Atwood et al. (2016) for details. Decomposition of energy fluxes was not performed for CSIRO due to the implementation of the volcanic forcing as a perturbation to the total solar irradiance (see text for details), while decomposition of LW feedbacks for HadCM3 wasn't performed due to limited data availability.

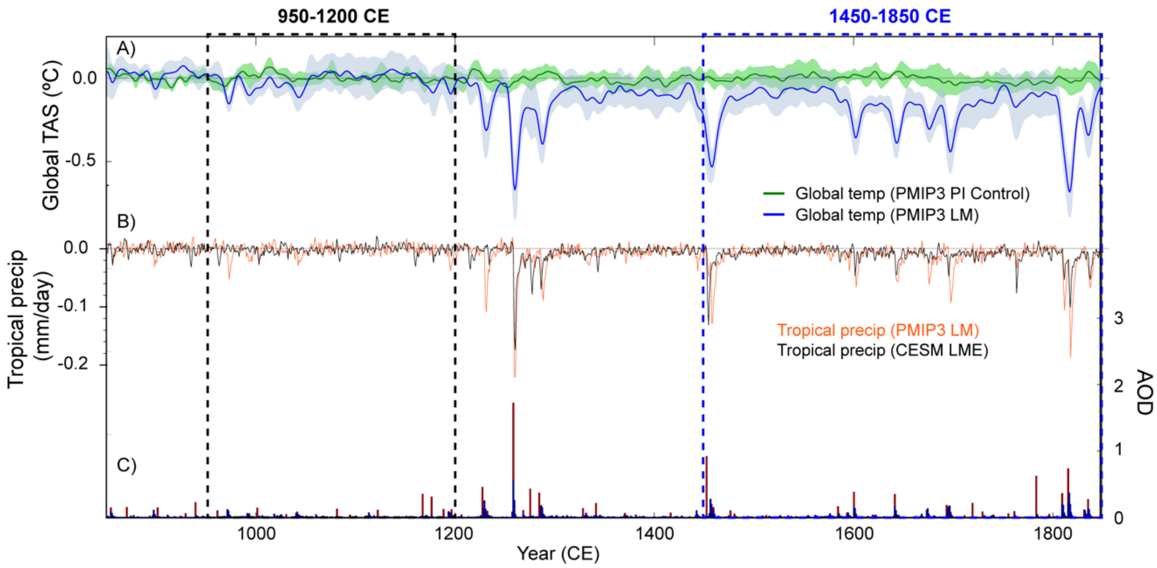

Figure S14. A) Multi-model mean global temperature anomaly in the PMIP3/CMIP5 last millennium and preindustrial control simulations, relative to first 150 years of each run. Shading represents the standard deviation in each set of runs. All data have been smoothed with a Gaussian filter (σ = 3 years). B) Multi-model mean tropical precipitation anomaly in the PMIP3/CMIP5 last millennium and the CESM Last Millennium Ensemble runs, area-weighted between 30ºS:30ºN, relative to first 150 years of each run. The tropical area-averaged precipitation change from the LIA to MCA is $\Delta P_{LIA-MCA}$ = -0.28 ± 0.08% [1σ] and -0.23 ± 0.04% for the CMIP5/PMIP3 LM and CESM LME runs, respectively, while the change only at the proxy sites is $\Delta P_{LIA-MCA}$ = -0.46 ± 0.36% and -0.12 ± 0.39%. C) Volcanic aerosol reconstructions used in the last millennium simulations, represented in terms of the aerosol optical depth (AOD) from Crowley et al. (2000) [blue bars] and estimated from Gao et al. (2008) [red bars] by dividing sulfate loading by 150 Tg (Stothers, 1984).

References

Donohoe, A., Marshall, J., Ferreira, D., McGee, D., 2013. The Relationship between ITCZ Location and Cross-Equatorial Atmospheric Heat Transport: From the Seasonal Cycle to the Last Glacial Maximum. J. Clim. 26, 3597-3618.

Kang, S.M., Held, I.M., Frierson, D.M.W., Zhao, M., 2008. The response of the ITCZ to extratropical thermal forcing: Idealized slab-ocean experiments with a GCM. J. Clim. 21, 3521-3532.